

# Prebiotic nanoscale cavity formation: GABA-induced exfoliation in Ca-montmorillonite

Orr Rose Bezaly,<sup>†,‡</sup> Annemieke Petrignani,<sup>\*,†</sup> and Helen E. King<sup>‡</sup>

<sup>†</sup>*Molecular Photonics, Van ‘t Hoff Institute for Molecular Sciences, Faculty of Science, University of Amsterdam, Science Park 904, 1098 XH Amsterdam, The Netherlands*

<sup>‡</sup>*Department of Earth Sciences, Faculty of Geosciences, Utrecht University, Princetonlaan 8a, 3584 CB Utrecht, The Netherlands*

E-mail: a.petrignani@uva.nl

Phone: +31 (0)20 5257158

## Abstract

We present exfoliation of a crystalline clay induced by the small carbon-chain amino acid,  $\gamma$ -aminobutyric acid (GABA), upon adsorption-desorption interaction. We experimentally investigated the interaction between Ca-montmorillonite clay (Ca-Mt) and GABA, a non-proteinogenic amino acid commonly found in carbonaceous meteorites. Despite evidence of only transient adsorption onto the clay surfaces, GABA exhibits the capacity to act as an exfoliator. ATR-FTIR spectroscopy reveals a non-reversible structural change of the Ca-Mt aluminosilicate network induced by GABA. Powder XRD analysis and TEM imaging reveal that localised, partial exfoliation of the clay layers occurs after interaction with GABA, creating internal nanoscale cavities in-between adjacent clay layers. These results demonstrate that an elementary, monomeric species can act as an exfoliating agent in a prebiotically-relevant scenario, and that in this process, nanoscale confined environments are formed. This work may

have far-reaching implications for the role of non-proteinogenic species in proteinogenesis (non-enzymatic formation of proteins) and for the role of clays in processes leading to the origin of life on rocky (exo)planets.

## Introduction

Since the first exoplanet ratification in 1992,<sup>1</sup> several thousands of exoplanets have been found, directing the field of prebiotic chemistry into a new era. The quest to decipher universal mechanisms for the origins of life on terrestrial planets is brought to the fore as we gain more knowledge of possible planetary environments in habitable zones beyond our Solar System.<sup>2</sup> One of the major hypotheses on origins of life on Earth is Darwin's warm little pond, set in Hadean times, around when first landmasses started to form.<sup>3,4</sup> In this warm pond scenario, that may be extended to other lifeless rocky planets, organics and minerals interact in a shallow water environment undergoing dry-wet cycling.<sup>5</sup> This primeval eon is also thought to have experienced extraterrestrial input of organics, with a period of significant meteoritic bombardment and dust influx.<sup>4</sup> Through this, off-world organics may be delivered to planetary surfaces, enriching the prebiotic planetary chemical inventory.<sup>6</sup> Meteoric and cometary dust studies reveal a fortitude of monomeric biomolecular building blocks, amongst which are a great variety of amino acids.<sup>7</sup> The contribution of off-world organics is specifically relevant to the sub-aerial warm pond setting.<sup>8</sup> Studying interactions of common off-world organics and abundant surface minerals is crucial for gaining insights into processes that shape prebiotic pond environments and more generally, on life as a universal phenomenon.

Clay minerals, presumed to be ubiquitous on rocky planets that have/had liquid water on their surface,<sup>9</sup> have a great affinity to adsorb organics and are known to catalyse chemical reactions.<sup>10,11</sup> They have been identified on Mars<sup>12</sup> and are expected to have also existed on early Earth.<sup>9</sup> Due to their extensive surface area and unique properties, clay surfaces are hypothesized to play a key role in prebiotic chemistry on lifeless worlds, where concentrations of organics are generally low and non-enzymatic catalytic functions are required.<sup>13</sup> Clay sur-

faces are regarded as a sink for certain protein-forming amino acids (termed 'proteinogenic'), locally increasing the amino acid concentration through adsorption. These proteinogenic amino acid-clay interactions have been widely investigated in the context of origins of life.<sup>14</sup> Particularly, the swelling clay montmorillonite (Mt) has chemical and structural properties that make it a favourable candidate for prebiotic surface chemistry (Figure 1). Using X-Ray Diffraction (XRD), the structure of Mt has been shown to swell and shrink reversibly under dry and wet conditions, possessing a basal spacing of 9.6 Å when completely dehydrated and up to 15 – 21 Å when its interlayer is saturated with water.<sup>15</sup> Under wet-dry cycling, oligomerisation reactions of proteinogenic glycine (adsorbed from 10 mM–1 M aqueous solutions) on Mt surfaces have been demonstrated to become energetically favourable, due to temporary lowering of the local water activity (the type of surface sites involved in this process is debated).<sup>16</sup> Under different conditions, a preferred heteropeptide oligomerisation in a system including L-Arginine and L-Glutamic acid adsorbed onto Mt has been reported.<sup>17</sup> Other studies, have demonstrated that Mt is able to catalyse RNA polymerisation,<sup>18</sup> where certain proteinogenic amino acids act as coenzymes.<sup>19</sup>

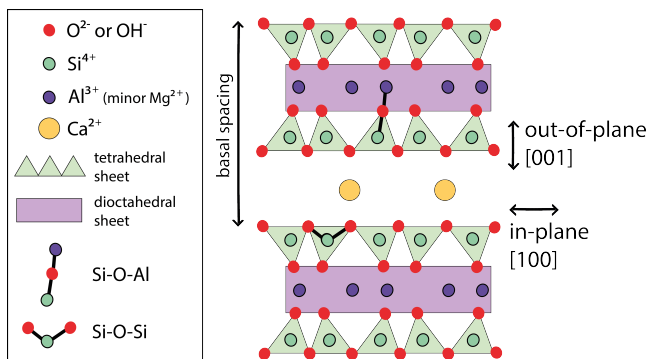


Figure 1: Schematic of Ca-Mt clay structure; a 2:1 aluminosilicate layered clay. The layered aluminosilicate units stack on top of each other to create a repetitive structure with interlayer spaces, where large cations ( $\text{Ca}^{2+}$  in this case) reside and balance the negatively charged basal siloxane surfaces. Also depicted are the orientations of the  $\text{Si}-\text{O}-\text{Al}$  and  $\text{Si}-\text{O}-\text{Si}$  stretching vibrations in relation to directions within the crystal structure.

Non-proteinogenic amino acids, despite their plentiful and universal characters, are less investigated and are often disregarded for their prebiotic relevance. However, non-proteinogenic amino acids may indirectly influence processes that contribute to organic complexity.  $\gamma$ -aminobutyric acid (GABA) is a small-sized ( $7 - 8 \text{ \AA}$ )<sup>20</sup> non-proteinogenic amino acid, that has been found to be present in similar concentrations to that of glycine in carbonaceous meteorites.<sup>21</sup> Hence the abundance of GABA in prebiotic times in warm pond settings could have been significant (with respect to other amino acids). GABA has been found to only weakly adsorb to clay surfaces (physisorption)<sup>22</sup> and therefore has been discarded from origins of life research, as it is deemed a non-viable competitor of proteinogenic amino acids. Interestingly, however, GABA is known to induce mineralogical modifications in aluminosilicate minerals such as zeolites, that also have exposed siloxane surfaces.<sup>20</sup> Information is lacking when it comes to understanding how clay properties may be affected by interactions with small monomeric building blocks, and more specifically, by meteorite-common, non-proteinogenic amino acids such as GABA.

One possible outcome of such organo-clay interactions is a structural change in the clay's layered structure, termed exfoliation. In this irreversible process, aluminosilicate layers are spatially separated from each other. Short peptides (a few monomers long) have been shown to induce exfoliation in Mt,<sup>23</sup> by being intercalated in the clay's interlayer spaces and forcing the aluminosilicate layers apart. Though widely investigated in material sciences,<sup>24</sup> clay exfoliation induced by interactions with organic building blocks and the associated structure and surface changes, are yet to be addressed in the field of origins of life.

In this paper, we report a study of the interaction of varying concentrations of non-proteinogenic GABA (100 mM–2 M) with a natural, well characterised calcium Mt clay (Ca-Mt). ATR-FTIR spectra are given to reveal possible interaction and/or any changes in chemical bonding in the GABA-exposed Ca-Mt. XRD patterns of clay samples provide structural information used to inspect the reversibility of observed effects. TEM imaging is employed to allow for direct observations of the clay structure after exposure to GABA.

## Results and discussion

Below the results of the GABA adsorption experiments onto Ca-Mt clay are presented. Measurements of GABA-exposed Ca-Mt samples after washing and drying ('exposed samples') and measurements of these samples after rehydration by only water vapour ('rehydrated samples') are shown (see Experimental, SI). First, the ATR-FTIR spectra of the samples exposed to different concentrations of GABA are given and discussed. FTIR spectra of GABA-exposed samples alongside rehydrated samples in the Si-O stretching region are treated and presented. Subsequently, powder X-Ray Diffraction (pXRD) measurements of d(001) peaks for GABA-exposed and rehydrated samples are given, investigating both possible structural changes in of Ca-Mt after GABA exposure and the reversibility of the clay's swelling. Finally, TEM imaging of rehydrated Ca-Mt samples is presented to unravel any physical changes to the clay's internal structure.

### Transient adsorption of $\gamma$ -aminobutyric acid

Figure 2 depicts the normalised ATR-FTIR spectra of GABA-exposed Ca-Mt samples (solid curves, grey to black with increasing GABA concentration), alongside a control sample (dashed curve). Figure 2a shows the normalised absorbance as a function of frequency for the full spectral range gathered ( $450 - 4000\text{ cm}^{-1}$ ). There are three regions of interest; I. fingerprint region of organics and OH bending modes  $1300 - 1700\text{ cm}^{-1}$  (Figure 2b), II. OH (and NH) stretching region  $3000 - 3700\text{ cm}^{-1}$  (Figure 2c), III. Ca-Mt clay absorbance region  $450 - 1250\text{ cm}^{-1}$  (Figure 2d). We focus on regions I and II to examine the extent of GABA adsorption and water content-related changes, and on region III to scrutinize changes in the chemical bonds of the mineral as a function of initial GABA concentration.

The intense peak at  $1640\text{ cm}^{-1}$  in region I (Figure 2b) is the OH bending mode of adsorbed water.<sup>25</sup> Most, but not all water is lost after dehydration of the GABA-exposed samples. Interestingly, the OH bending intensity decreases with increasing GABA concentration, in-

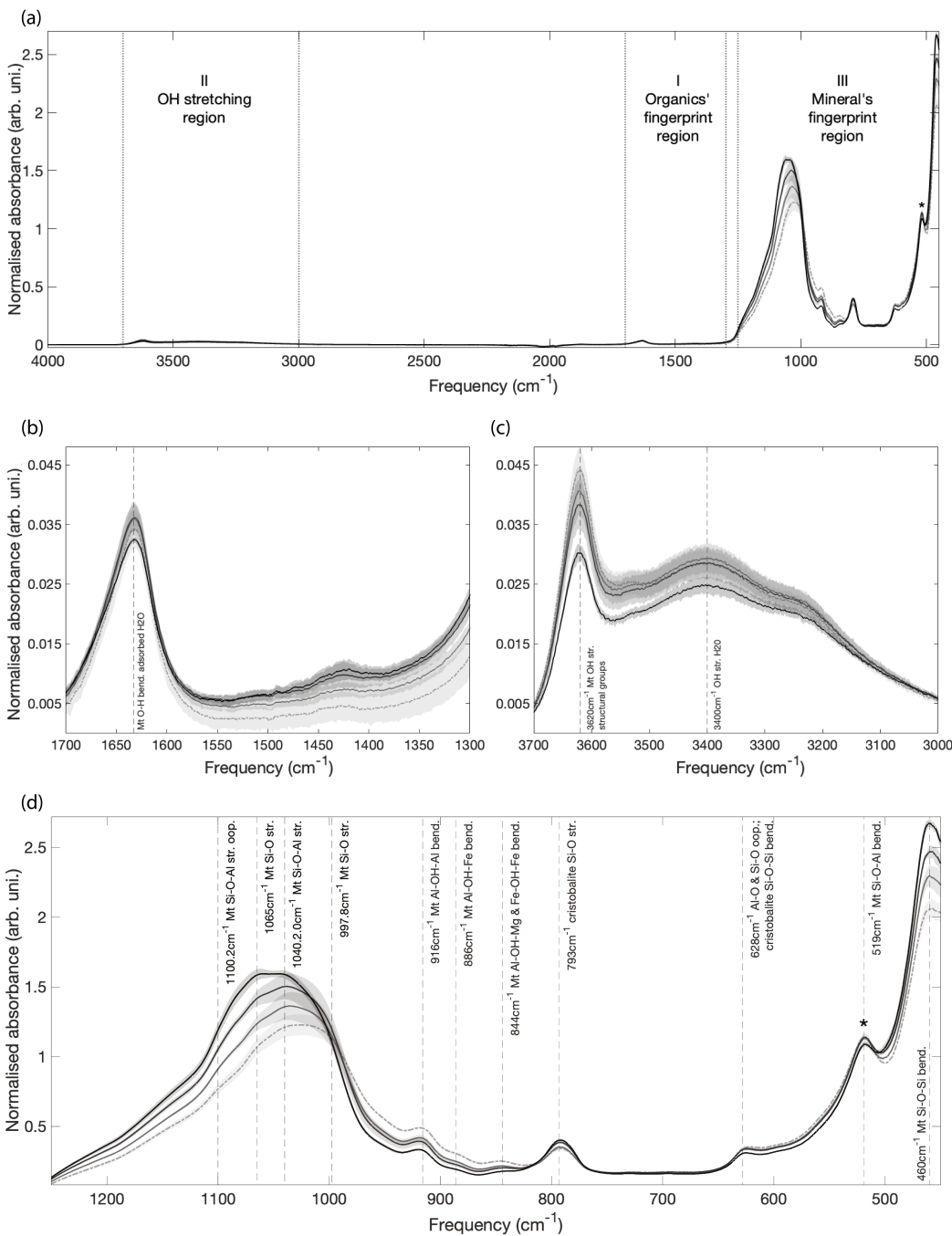


Figure 2: Normalised ATR-FTIR spectra of dehydrated Ca-Mt clay after interaction in MilliQ water without GABA (control, dot-dashed) and with 400 mM, 700 mM and 2 M GABA (light grey to black, respectively). Each spectrum is an average of three experimental repetitions. The highlighted margins represent the corresponding standard deviations. Each spectrum is normalised to the fitted band (asterisk) at 519  $\text{cm}^{-1}$  (see Experimental). (a) The full spectral range 450 – 4000  $\text{cm}^{-1}$ , divided into three (I-III) interest regions: (b) organics' fingerprint region I 1300 – 1700  $\text{cm}^{-1}$ , (c) OH stretching region II 3000 – 3700  $\text{cm}^{-1}$ , and (d) mineral's fingerprint region III 450 – 1250  $\text{cm}^{-1}$ . Band assignments based on Ca-Mt control are given in dashed vertical lines. Str. = stretching, bend. = bending, oop. = out-of-plane.

dicating less water is retained in the dehydrated clay after it was exposed to GABA. This is most apparent after exposure with 2 M GABA concentration. The weak spectral feature centered at  $1425\text{ cm}^{-1}$  originates from the mineral sample itself, as also observed in the control sample. There is no indication of GABA itself being absorbed. Any GABA fingerprints would be expected around 1579, 1398 and  $1309\text{ cm}^{-1}$ .<sup>26</sup>

In region II (Figure 2c), two main spectral features related to OH stretching can be found; a broad feature around  $3400\text{ cm}^{-1}$  attributed to adsorbed water molecules and narrower a band at  $3620\text{ cm}^{-1}$  related to OH stretching of OH groups within the clay's structure.<sup>25</sup> Similar to the OH bending band of the clay in region I, the  $3400\text{ cm}^{-1}$  band also decreases with exposure to increasing GABA concentrations, confirming the clay drying more easily after increased exposure (Figure 2c). Also similar to region I, there are no features pointing to any GABA absorption. Although the  $3410\text{ cm}^{-1}$  fingerprint of GABA could possibly be obscured by the dominating OH bands, there is also no indication of any GABA absorption around  $3028\text{ cm}^{-1}$ .<sup>26</sup> GABA molecules (predominantly in the zwitterionic state at these experimental conditions<sup>27</sup>) are expected to interact via electrostatic interaction with the negatively-charged siloxane surfaces of Ca-Mt. The absence of any GABA bands in the exposed samples demonstrates that GABA does not remain adsorbed to the surfaces of Ca-Mt after washing (see SI for ATR-FTIR spectra of water washes of GABA-exposed Ca-Mt), even at the highest concentration examined. This finding is consistent with the known weak-adsorption behaviour (physisorption) of GABA on clay surfaces.<sup>22</sup>

Although GABA does not remain at the mineral surface after washing, major changes are observed in IR bands related to the mineral in region III (Figure 2d). Here, there are multiple bands associated with the clay's atomic structure, particularly, Si-O stretching ( $950 - 1150\text{ cm}^{-1}$ ) and bending ( $450 - 550\text{ cm}^{-1}$ ) modes, and OH bending modes connected to different cations within the clay's structure such as Al, Mg and Fe.<sup>25,28</sup> Moreover, there are two bands associated with cristobalite, one of the silica polymorphs that constitute about 25% of the natural clay material used in this study.<sup>25</sup> The most marked change in the ATR-

FTIR spectral region III (Figure 2d), is in the shape of the broad envelope created by the overlapping Si-O stretching bands. Here an increasing shift in the maximum of the envelope to higher wavenumbers is observed as a function of increasing initial GABA concentration. Other bands of Ca-Mt are also observed to change in response to GABA exposure, with the changes being most prominent with maximum GABA exposure. The bending vibration of Si-O-Si at  $460\text{ cm}^{-1}$ , associated with the silica tetrahedral layers, increases in intensity with increasing GABA concentration. Intensities of the Al-OH-Al bending at  $916\text{ cm}^{-1}$ , the Al-OH-Fe bending at  $886\text{ cm}^{-1}$ , and the Al-OH-Mg and Fe-OH-Fe bending at  $844\text{ cm}^{-1}$  decrease with increasing GABA-concentration exposure. Changes in Si-O stretching and bending bands are closely related to the structural state of the clay's aluminosilicate network<sup>29</sup> and can reflect a structural alteration of Ca-Mt (Figure 1). The dependency of the alterations on the GABA concentration and these alterations persisting even though no lasting GABA adsorption is observed, point to a transient GABA-Mt interaction.

## Local structure changes in Ca-montmorillonite layers

The nature of the structural changes can be further investigated by looking more closely to the behaviour of the Si-O stretching band envelope at  $950 - 1150\text{ cm}^{-1}$ . A peak-finding procedure was applied to the Si-O stretching region to find and fit the individual vibrational mode contributions and plot their positions as function of initial GABA concentration (see Experimental). The modes of both exposed (black) and rehydrated (blue) Ca-Mt samples were analysed. Figure 3 shows the ascertained band frequencies of two Si-O-Al (out-of-plane and in-plane) modes and two Si-O-Si (in-plane) modes as function of initial GABA concentration. The out-of-plane Si-O-Al band position around  $1098\text{ cm}^{-1}$  is displayed in Figure 3a. In the case of the GABA-exposed Ca-Mt samples (black), its position is red shifted by approx.  $14\text{ cm}^{-1}$  for high GABA concentrations with respect the control sample. On the contrary, its in-plane counterpart does not change, even for the highest GABA concentration (Figure 3b). The positions of the in-plane Si-O-Si bands are not (Figure 3c)

or only slightly affected (Figure 3d). The change in the out-of-plane Si-O-Al mode, whilst its in-plane counterpart remains unaffected, points to a change in the [001] direction (Figure 1) and suggests a structural alteration of Ca-Mt<sup>30</sup> induced by the interaction with GABA.

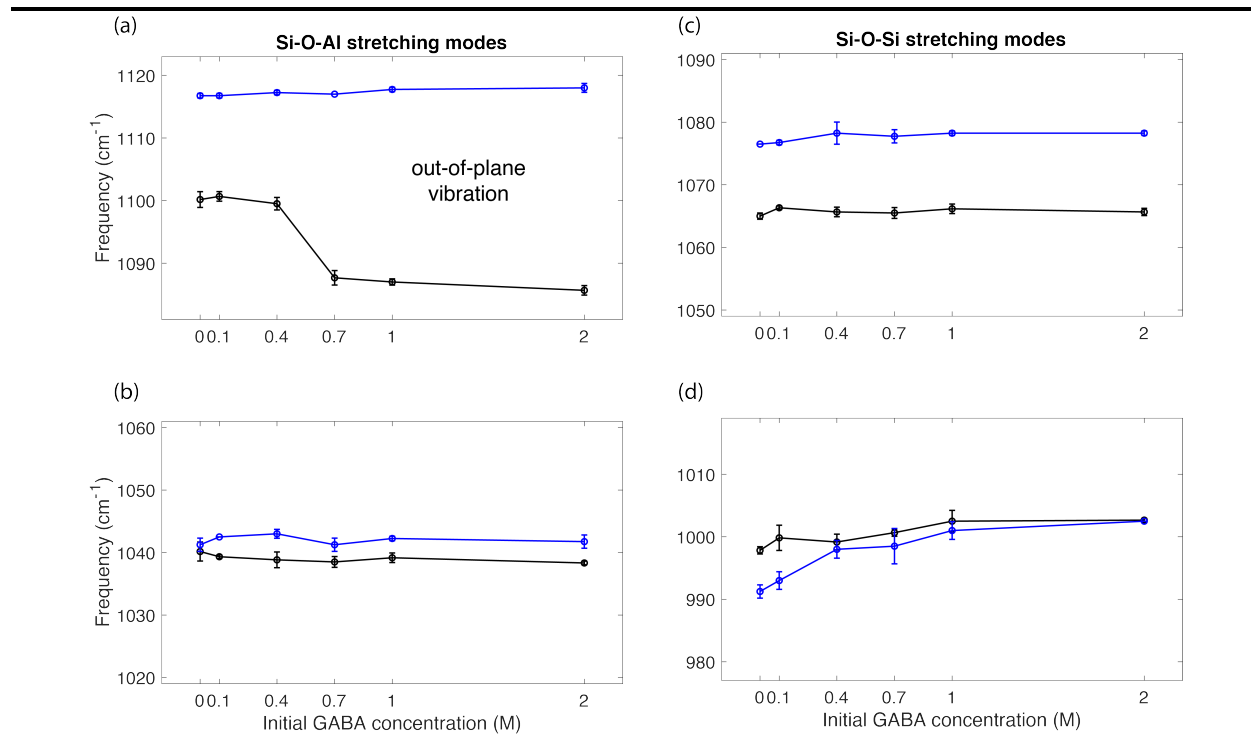


Figure 3: Si-O stretching vibration frequencies of Ca-Mt as a function of initial GABA concentration for dehydrated GABA-exposed samples (black) and rehydrated samples (blue). Si-O-Al stretching modes around (a)  $1100\text{ cm}^{-1}$ : out-of-plane, (b)  $1040\text{ cm}^{-1}$ : in-plane. Si-O-Si stretching modes around (c)  $1070\text{ cm}^{-1}$ : in-plane (higher-frequency), (d)  $1000\text{ cm}^{-1}$ : in-plane (lower-frequency). See Figure 1 for an illustration of these Si-O stretching modes in Ca-Mt structure. All y-axes have a range of  $42\text{ cm}^{-1}$ .

Introducing water molecules back into the altered Ca-Mt effectively masks the frequency shift in the perpendicular direction that is observed for the exposed samples (Figure 3a, blue line). Notably, the small shift in the Si-O-Si stretching lower-frequency mode of the dried, exposed sample becomes accentuated upon re-adsorption of water (Figure 3d). The shift of the mode is correlated with GABA concentration and cannot be due to differing water uptake, as the water weight gain is controlled to be similar for all samples in the rehydration step (see SI). Thus, even after rehydration, the change that GABA induces in

the structure of Ca-Mt is retained. The Si-O-Si in-plane stretching modes are internal modes occurring within the tetrahedral sheets (Figure 1). Any disruption induced by either water or GABA is expected to affect these bands. As only the lower-frequency Si-O-Si stretching band seems to be affected by exposure to GABA, this confirms that the Si-O-Si network is being disrupted, but only locally and not significantly enough to disrupt both Si-O-Si vibrational modes (Figures 3c, d). In summary, the GABA-altered Ca-Mt samples maintain their structural alteration upon rehydration, thus pointing towards an irreversible process that has taken place. These irreversible effects should be observable in other behaviours that depend on interactions of the clay's siloxane surfaces, such as in the reversibility of the swelling behaviour of Ca-Mt.

## Irreversible alteration of Ca-montmorillonite layered structure

Complementary to ATR-FTIR data, XRD data of Ca-Mt provides long-range structural information for both the [001] direction that is perpendicular to the clay layers and the periodicity of the structure in other lattice directions. The clay's response to water adsorption and its reversible swelling capacity is hereby examined for GABA-altered samples. Figure 4a presents the normalised XRD d(001) peak of GABA-exposed samples, for 2 M GABA-altered Ca-Mt samples (black) and control Ca-Mt samples (unexposed to GABA, grey dot-dashed). For full pXRD patterns acquired see SI. The d(001) peak of the control sample is asymmetric, wide and of relatively low intensity (Figure 4a). The behaviour of the control sample is consistent with the literature documented behaviour of Ca-Mt upon dehydration.<sup>15</sup> Dehydration of Ca-Mt results in intensity loss and shape change (flattening and asymmetric widening) of the XRD d(001) peak due to water loss from the interlayer spaces and their consequent collapse. After GABA exposure, a change in the pattern of the d(001) peak is observed. The 2 M GABA-altered Ca-Mt sample exhibits an even more diminished peak compared to that of the control sample. Lack of a peak shift or increase in intensity with respect to the control sample, reiterates that GABA did not remain within the clay's interlayer spaces.<sup>31</sup> In other

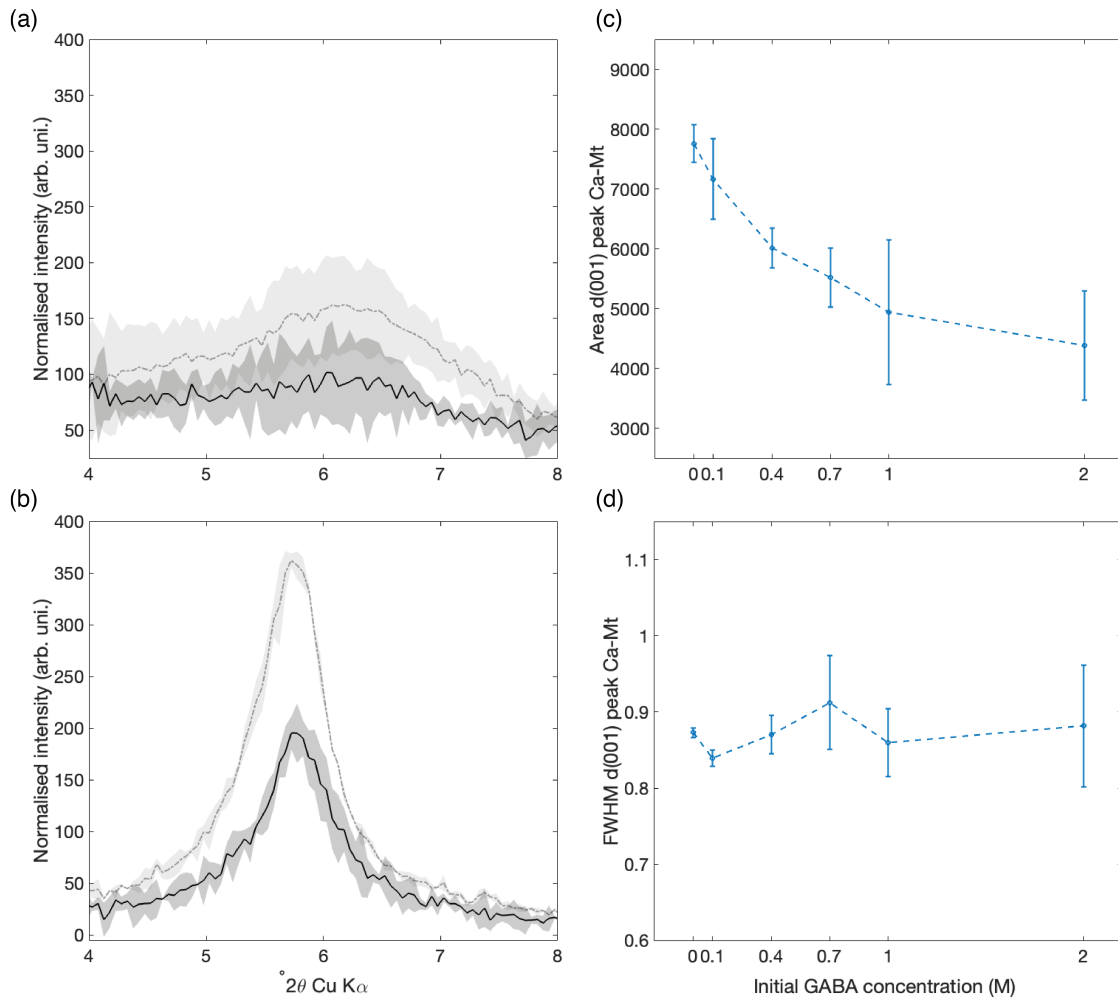


Figure 4: Normalised XRD d(001) peak of Ca-Mt exposed to 2 M GABA (black) and Ca-Mt control sample (dot-dashed grey) for (a) dehydrated and (b) rehydrated samples. Diffractograms are normalised to the area of a specific control sample's d(105) diffraction peak in the range  $34.5 - 39(\theta)$  (see Experimental and SI). The curves are generated by averaging diffractograms of experiment repetitions. The derived standard deviations are illustrated by highlighted margins around the curves. The (c) area and (d) FWHM of the rehydrated Ca-Mt d(001) diffraction peaks as function of GABA-concentration exposure are also given as a function of initial GABA concentration.

words, the absence of the Ca-Mt d(001) peak, confirms that GABA is not intercalated in the interlayer spaces of Ca-Mt after washing and points to only transient adsorption. This is consistent with ATR-FTIR findings that show no signs of GABA adsorption onto Ca-Mt basal surfaces after the washes (Figures 2b, c). Moreover, further weakening of the already weak XRD d(001) peak after exposure to 2 M GABA concentration, reiterates the lower retention of water in comparison to the control sample. This is consistent with ATR-FTIR findings that show a decreased intensity of adsorbed water band around  $3400\text{ cm}^{-1}$  (Figure 2c). In short, water is more effectively lost from the 2 M GABA-altered sample, resulting in the lower intensity of the water FTIR bands and d(001) peaks compared to the control sample.

Figure 4b shows the normalised XRD d(001) peak of 2 M GABA-altered Ca-Mt samples (black) and control Ca-Mt samples (unexposed to GABA, grey dot-dashed) after rehydration. As expected, re-adsorption of water in the Ca-Mt control sample results in the reappearance of the d(001) peak, demonstrating the clay's reversible swelling behaviour.<sup>15</sup> Intriguingly, this is not the case for the 2 M GABA-altered Ca-Mt. This sample does not recover its d(001) peak to the same intensity as the control sample. To assess this effect, the area of the d(001) peaks and the Full Width Half Maximum (FWHM) as a function of initial GABA concentration are examined for the rehydrated samples and presented in Figures 4c, d, respectively. While the area of the d(001) peak significantly decreases, the FWHM of the peak does not change as a function of the initial concentration (even though the standard deviation increases). As the intensity of the d(001) peak in the 2 M GABA-altered sample is not restored to control sample levels, our results indicate that the GABA-induced structural change of Ca-Mt suppresses its reversible swelling capacity. No significant changes in other lattice directions are observed, including the [100] direction (see SI). Concomitantly, the results suggest that the long-range crystal periodicity in the [001] direction is not completely destroyed, as the d(001) peak is partially regained, even after the GABA-induced alteration. Given the FTIR results that show a shift of internal vibrational modes and reflect local

changes in the Ca-Mt mineral, both techniques together suggest that the changes induced by GABA are very local in the (001) surfaces, but that these can have a large effect on the material properties of Ca-Mt.

Reduction in the intensity recovery of the d(001) peak in the pXRD upon rehydration of GABA-exposed Ca-Mt (Figure 4c) could be related to (partial) exfoliation of the clay.<sup>32</sup> Another, independent indication for clay exfoliation, arises from the FTIR analysis that reveals shifts of the out-of-plane Si-O-Al vibrational mode (Figure 3a) associated with this particular structural alteration.<sup>30</sup> Clay exfoliation is further associated with an enlargement of outer-surface area at the expense of interlayer surfaces.<sup>29</sup> We observe signs for this effect, as water loss upon dehydration is easier in the GABA-exposed clay compared to the control sample, according to FTIR spectra and XRD data. Exfoliation has been observed with a range of clay materials and organic molecules,<sup>24</sup> including some few monomers-long peptides.<sup>23</sup> However, in this work we observe exfoliation after merely a transient adsorption of a small-sized organic molecule, namely in the presence of GABA in water without preceding chemical treatment. Previous works report that exfoliation is also associated with increasing XRD d(001) values, originating from the retention of large organic compounds within the clay structure, and increase in FWHMs of the XRD peaks due to micro-stresses<sup>23</sup> or formation of particles smaller than 50 nm.<sup>33</sup> Here, however, we observe a different behaviour, suggesting a different exfoliation mechanism is in play. Short carbon-chain amino acids (up to 8-carbons, 24 mM) with a terminal amino group are thought to lie flat within the interlayer space,<sup>34</sup> limiting their ability to cause exfoliation. Still, our pXRD results and FTIR analysis strongly point to (partial) exfoliation of Ca-Mt occurring, induced by transient interaction with GABA. Therefore, we present below Transmission Electron Microscopy (TEM) imaging to directly observe and characterise the exfoliation in the Ca-Mt samples after alteration through interaction with GABA molecules.

## Partial exfoliation and nanoscale cavity formation

Figure 5 presents TEM images of the rehydrated samples. Figure 5a shows an image of the Ca-Mt control sample, which exhibits features of ordered 2:1 aluminosilicate layers visible as equally spaced dark lines, alongside material with a cloudy and/or granular appearance. This image is an example of a grain with nicely ordered layering. Some images of the control sample exhibit slightly distorted layering (see SI). Figure 5b presents a 2 M GABA-altered Ca-Mt sample (with equal water weight gain upon rehydration, see SI). Remarkably, multiple nanoscale cavities can be observed. These are found in between adjacent (distorted) aluminosilicate layers. The cavities are estimated to form in a significant percentage of the grains, up to 25%, after the GABA exposure (see SI). No cavities are found in the control Ca-Mt sample. The nanoscale cavities are always accompanied by distorted layering, which also appears more often after exposure (see SI). The cavities have an average size of  $3.08 \pm 1.66$  nm in the [001] direction, with the smallest and largest cavity possessing a respective size of  $1.35 \pm 0.20$  nm and  $6.30 \pm 0.31$  nm. Surprisingly, these nanoscale cavities are observed to occur mid-layer, predominantly embedded within the interior of the sheet structure, and not restricted to the edges where the sheets terminate.

TEM imaging not only confirms GABA-induced (partial) exfoliation is taking place, but goes beyond it to show that in this process, local nanoscale cavities are formed mid-layer within the distorted aluminosilicate layered structures. The direct observation of these nanocavities confirms the ATR-FTIR and pXRD results presented in this study, which indicate localised, irreversible structural changes occur. Note that no absorbance peak is observed at  $3691\text{ cm}^{-1}$  (Figure 2c), which is characteristic of the 1:1 clay kaolinite.<sup>28</sup> This suggests that the 2:1 aluminosilicate layers remain intact in the exfoliation/cavity formation process. Yet, due to the exfoliation, there is a loss of coherency of the layered structure of Ca-Mt, predominant in the direction perpendicular to the layers (the [001] direction). This is physically manifested by the formation of local nanoscale cavities, visible by TEM imaging.

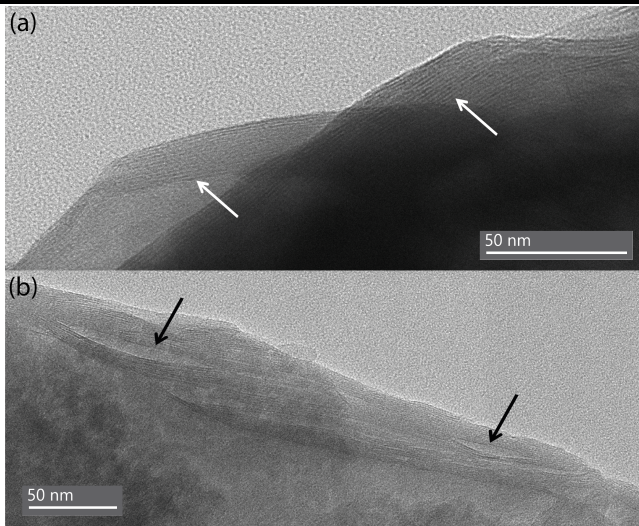


Figure 5: TEM images of rehydrated Ca-Mt (water weight gain 18%): (a) control sample, where white arrows mark well-ordered aluminosilicate layers and (b) 2 M GABA-altered sample, where black arrows indicate a couple of the nanoscale cavities between adjacent aluminosilicate layers.

---

The (partial) exfoliation seems to originate from the transient interaction character of GABA with Ca-Mt. This character can also allow for GABA recycling, which might explain the localised, interior appearance of the cavities. A single GABA molecule can then repeatedly damage the clay structure at the same area and do so for a longer time when it is located mid-layer. The recycling would lead to a local self-amplification effect, bringing about the partial exfoliation. Even at GABA concentrations lower than 2 M, for example at 400 mM, the effects are already observable in the FTIR spectra (Figures 2d, 3d) and XRD data (Figure 4c), for a contact time as short as two-hours. Therefore, a striking possibility is that even when considering the low organic concentrations expected in prebiotic environments (presumably only up to few mM), this self-amplified alteration effect on the clay's structure observed in this study can possibly not be neglected.

The formation of nanoscale cavities within the Ca-Mt clay can have far-reaching impact. The physicochemical conditions in these (semi-)confined cavities could dramatically differ from the external conditions. For example, binding of water within the interlayer space of a clay has been found to significantly decrease its melting/freezing temperature, resulting in

the presence of supercooled water. This effect was observed in Mt,<sup>35</sup> and in other clays such as halloysite<sup>36</sup> and vermiculite.<sup>37</sup> While in these studies, 2D confinement of water was investigated, computational work has shown that nano-pores can hold bound, unfreezable water up to a pore size of  $2.3 \pm 0.1$  nm.<sup>38</sup> It is not experimentally known how dissolved/adsorbed organics influence this behaviour, but these nano-scaled cavities with bound water activity could promote polymerisation reactions as lowered water activity is a requirement.<sup>16</sup> The nano-scaled pores also allow for localised organic concentrations, pH (also influenced by the presence of organics), and other parameters that are different from the outside conditions. This positions the nanoscale cavities in a non-equilibrium state with respect to the external environment, a required starting point for many life-relevant processes.

Our results shed new light on processes that organo-clay interactions with exogenous organic species can induce. GABA is a non-proteinogenic, predominantly meteoric species. It is not expected to undergo polymerisation, yet our results reveal the importance of incorporating such organic species in origins-of-life research and the possible importance of exogenous delivery. This work illustrates that an exogenous species can significantly change the physicochemical nature of the surface clay. The transient GABA-induced interaction irreversibly alters the Mt swelling clay, resulting in the formation of nanoscale cavities and a suppressed swelling capacity, paving the way to more complex surface-catalysed chemistry.

## Conclusion and Outlook

This work provides fundamental insights into processes that may play a key role in prebiotic warm rock pool environments, exemplifying that structural changes in clay can be induced by interactions between small organics and these minerals. GABA, a meteoric, non-proteinogenic amino acid, is experimentally found to act as an exfoliating agent of Ca-Mt upon its transient adsorption under prebiotically-relevant temperatures and mild conditions. The nature of the GABA-Mt interaction is transient, yet the alteration of Ca-Mt is irreversible. GABA induces (partial) exfoliation, leading to the formation of local, nanoscale cavities between adjacent aluminosilicate layers. This causes loss of layer coherency and suppression of the reversible swelling capacity of the clay. The local, non-edge defects influence the properties of the material predominantly in the direction perpendicular to the clay layers and can be detected by analysing the IR signatures of the dehydrated clay. The localised character and interior placement of the partial exfoliation points to an amplification effect with the GABA being recycled (repeatedly adsorbed and desorbed) before being lost. These further suggest that the GABA-induced exfoliation behaviour of Ca-Mt is inherently different compared to other, well-investigated, clay exfoliation mechanisms. The formation of nanoscale cavities could be of major importance to origin-of-life research, and might have indirect implications on proteinogenesis on rocky (exo)planets. The emergent nanoscale cavities are (semi-)confined nano-environments inside the clay's layered structure, in which conditions may differ significantly compared to the external environment (e.g. change in water activity, pH, increased organic concentrations). Further research is needed in order to elucidate the mechanism governing the exfoliation process and to investigate the possible importance to the origins of life on rocky planets.

## Experimental

Calcium montmorillonite STx-1b (Ca-Mt) source clay was purchased from the Clay Mineral Society, USA. The chemical formula of STx-1b is



and the cation exchange capacity value is  $66.1 \pm 2.1$  100meq/100gr.<sup>25</sup> The fine clay fraction with a diameter  $\leq 2 \mu\text{m}$  was separated by sedimentation in ultrapure Milli-Q water (18.2 MΩ\*cm @25°C, 1.5ppb TOC), where the settling velocity was calculated according to Stokes law. After sedimentation, the clay was dried in an oven at 180°C in air for at least one week. The sedimentation procedure was confirmed successful using SEM imaging. This fine clay fraction was then used throughout the experiments. γ-aminobutyric acid (GABA) ( $\geq 99\%$ ) was purchased from Sigma-Aldrich and used without further purification.

## Experimental procedure

Ca-Mt-GABA suspensions were prepared in the following fashion: GABA solutions of concentrations 100 mM, 400 mM, 700 mM, 1 M and 2 M in Milli-Q water were added to Ca-Mt in the ratio of 3 mL solution per 100 mg clay. The pH of the GABA solutions was not adjusted. pH was measured at room temperature using a Mettler-Toledo pH probe calibrated with standard solutions (see SI). The control experiments with Ca-Mt water suspension were conducted with Milli-Q water, thus did not contain any GABA. All suspensions were stirred at a rate of 650 rpm whilst retained at 80°C for two hours ('suspension-adsorption' step) in 10 mL glass vials that were loosely covered with pierced aluminium foil to prevent water evaporation. The suspensions were then separated by centrifugation at 3000 rpm for 5 minutes and the supernatant was collected. The remaining solid clay samples were washed twice by re-suspending the solids in about 5 mL of Milli-Q water, followed by shaking at 1000 rpm for 15 minutes, after which the samples were centrifuged at 2500 rpm for 5 minutes, enabling the collection of the washed supernatants (see SI). The twice-washed solid clay samples

were dehydrated at 120°C in an oven with the fan function on (i.e. under flowing air) for 163 hours and 40 minutes (samples that have undergone this treatment are referred to as 'exposed samples'). Three separate experimental repetitions of the suspension-adsorption procedure followed by washes and dehydration, as described above, were performed on different occasions. For two of these repetitions, that took place at two consecutive days, the same GABA 2 M stock solution was used. The third repetition, that took place at a later occasion, required the preparation of a new stock solution.

Rehydration procedure: Dehydrated solid samples of control and GABA-exposed Ca-Mt were rehydrated by humidification with water vapour generated from MilliQ water in a sealed box until a weight gain of about 15-30% was measured (so called 'rehydrated samples'). Two rehydration sets were performed, using GABA-exposed and control Ca-Mt samples from two respective experimental repetitions. The humidification time was 24 hours for the first set and 6 hours for the second set. For each rehydrated clay sample, the ratio of weight of adsorbed water to weight of dehydrated clay ('adsorbed water weight gain') was calculated.

## Attenuated Total Reflectance Fourier Transform InfraRed Spectroscopy

ATR-FTIR measurements were carried out using a Perkin Elmer FT-IR spectrometer "Frontier" with a "GladiATR" mount (Pike technologies). The ATR mount was connected to a nitrogen/air flow in over-pressure starting at least 30 min before measuring. The measurements of solid samples were carried out with a resolution of  $2\text{ cm}^{-1}$  (data interval  $0.5\text{ cm}^{-1}$ ), and were a composite of 64 scans that were accumulated over a spectral range of  $450 - 4000\text{ cm}^{-1}$  at room temperature. A background scan was collected before each solid sample measurement. The measurements of liquid samples were carried out using the same resolution, but by accumulating 8 scans in the spectral range of  $450 - 4000\text{ cm}^{-1}$  at room temperature. A background scan was collected after every 4 – 5 liquid samples.

Baseline subtraction was carried out by first identifying the baseline using a linear fit of

spectral ranges in which no absorbance bands were expected nor observed, namely between  $2400 - 2800\text{ cm}^{-1}$  and  $3800 - 4000\text{ cm}^{-1}$ . The linear fit was then subtracted from the entire spectrum. Peak position determination was performed using second derivative analysis.<sup>39</sup> To obtain a usable second derivative plot it was necessary to smooth the data within our regions of interest, a common practise for this type of analysis.<sup>40</sup> The data was smoothed using a second order Savitsky-Golay filter<sup>41</sup> with a 31-point window. This allowed us to calculate the first derivative curve, which was also smoothed in the same manner, to determine the second derivative plot of each spectrum. The points that define a minimum in this plot correspond to absorbance-band positions and were identified using a Matlab script. The peak finding procedure was applied to the (greater range of the) Si-O stretching band envelope at  $885 - 1285\text{ cm}^{-1}$  and to the range of  $450 - 660\text{ cm}^{-1}$ , that includes the Si-O-Al bending mode at  $519\text{ cm}^{-1}$  selected for normalisation. The  $519\text{ cm}^{-1}$  mode was selected as it represents the in-plane vibrational mode furthest from the interlayer space, that is assumed to be least affected by interactions of the basal siloxane surfaces. For intensity-normalisation to this mode, a fitting procedure employed Gaussian functions at the derived band positions (including position uncertainty of  $\pm 4\text{ cm}^{-1}$  for dehydrated samples and  $\pm 6\text{ cm}^{-1}$  for rehydrated samples) in the range of  $450 - 660\text{ cm}^{-1}$  with band widths of  $26 \pm 4\text{ cm}^{-1}$ . The final spectra are averaged spectra of available experimental repetitions with the standard deviation as function of frequency displayed as highlighted margins around the averaged curves.<sup>42</sup>

## Powder X-Ray Diffraction

pXRD measurements were carried out using a Rigaku MiniFlex II diffractometer with a Ni-filtered Cu K $\alpha$  source ( $\lambda=1.540562\text{ \AA}$ ) operated at voltage of 30 kV and current of 15 mA. For X-ray detection, a NaI(Tl) scintillation detector with a Be window of diameter  $\phi 23\text{ mm}$  and length of 80 mm was used. A single-crystal silicon low background sample holder with a 0.2 mm deep and 8 mm diameter cavity was used. Powder samples were ground then pressed into the cavity in the sample holder to create a flat and uniform surface, excess material

was removed. All measurements were carried out in the range of  $3 - 40(^{\circ}2\theta)$ . In the ranges of  $3 - 10(^{\circ}2\theta)$  and  $34 - 40(^{\circ}2\theta)$ , measurements were carried out in  $0.01^{\circ}$  resolution with scanning rate of  $0.5^{\circ}/\text{min}$ . In the range of  $10 - 34(^{\circ}2\theta)$  they were carried out typically in  $0.05^{\circ}$  resolution and rate of  $2.5^{\circ}/\text{min}$ , and for a few samples in resolution of  $0.01^{\circ}$  and rate of  $0.5^{\circ}/\text{min}$ .

Background measurements that were gathered on the same day as the sample measurements were smoothed using a 21-point moving average and subtracted from each diffractogram. Diffraction data obtained with a resolution of  $0.01^{\circ}$  were binned to  $0.05^{\circ}$  resolution to increase the signal-to-noise ratio. The diffractograms were area normalised to the Ca-Mt d(105) peak in the range of  $34 - 39.5(^{\circ}2\theta)$  of one of the control samples. Normalisation was conducted separately for the GABA-exposed and rehydrated clay data sets. The Mt d(105) peak was chosen for normalisation in all cases, as it did not change shape and position for different samples. The final diffractograms are averaged diffractograms of available experimental repetitions with the standard deviation as function of  $^{\circ}2\theta$  value displayed as highlighted margins around the averaged curves.<sup>42</sup> The d(001) diffraction peaks of Ca-Mt were fitted to Lorentzian functions<sup>43</sup> of the form  $y = P_1/((x - P_2)^2 + P_3) + C$  in the range of  $4 - 8(^{\circ}2\theta)$ . The FWHM of each Ca-Mt d(001) peak was derived using the fit parameter  $P_3$  according to  $FWHM = \sqrt{4P_3(1+s)}$  (following equation 21 in ref<sup>44</sup>), where  $s$  is the asymmetry factor, chosen have a value of 0.5 for all peaks. The area of each Ca-Mt d(001) peak was obtained by integrating over the fitted Lorentzian function.

## Electron Microscopy

TEM imaging was performed using a Thermo Fischer TFS Talos F200X S(TEM) instrument, at an accelerating voltage of 200kV. Rehydrated Ca-Mt samples (control and GABA 2 M-interacted) with 18% weight gain due to water adsorption were examined. Image analysis was performed using ImageJ program. We analysed 29 images of the 2 M GABA-altered sample and 16 images of the control sample (see SI). To determine average basal spacing for each

sample, we analysed images exhibiting both well-ordered and distorted layered structures, excluding cavities. To quantify the occurrences where well-ordered vs. distorted 2:1 layered structures appeared, we manually selected and categorised all the available TEM images where at least 4-5 adjacent layers were clearly visible (not including image multiplicity). For ordered/distorted categorisation, in cases where a distorted layered structure was observed the image was counted as 'distorted' even if an ordered structure was present at another part of that image (i.e. not counting a single image twice). This was performed for both control and 2 M GABA-altered rehydrated samples. Cavity size determination was performed by measuring the cavity size in the [001] direction ten times for the same cavity and calculating the average and standard deviation. A total number of ten cavities were analysed, observed in seven different images.

## Acknowledgement

This study is supported by NWO grant of the Planetary and Exoplanetary Science programme (PEPSc.19.009) of A.P. and H.E.K. The authors thank Dr. O. Lugier and the Functional Materials lab of Dr. S. Grecea (UvA), Dr. G. Giubertoni (UvA), D. van Erp (UvA), Dr. M. Hamers (UU) and the Molecular Photonics group at UvA.

## Supporting Information Available

Rehydration of GABA-exposed Ca-Mt (Table S1); ATR-FTIR spectra of MilliQ water washes of GABA-exposed Ca-Mt (Figure S1); ATR-FTIR spectra of rehydrated Ca-Mt samples after GABA exposure: Full spectral range and mineral's absorbance region (Figures S2, S3); Full range pXRD measurements of GABA-exposed and rehydrated Ca-Mt samples (Figures S4, S5); Additional TEM images: distorted layered structures in rehydrated Ca-Mt control and 2 M GABA-altered samples (Figure S6); TEM images analysis of rehydrated Ca-Mt control and 2 M GABA-altered samples (Table S2); pH of GABA solutions (Table S3);

## References

- (1) Wolszczan, A.; Frail, D. A. A planetary system around the millisecond pulsar PSR1257+ 12. *Nature* **1992**, *355*, 145–147.
- (2) (a) Brady, M. T.; Bean, J. L. Assessing the transiting exoplanet survey satellite's yield of rocky planets around nearby M dwarfs. *Astron. J.* **2022**, *163*, 255; (b) Claringbold, A.; Rimmer, P.; Rugheimer, S.; Shorttle, O. Prebiosignature molecules can be detected in temperate exoplanet atmospheres with JWST. *Astron. J.* **2023**, *166*, 39; (c) Miles, B. E.; Biller, B. A.; Patapis, P.; Worthen, K.; Rickman, E.; Hoch, K. K.; Skemer, A.; Perrin, M. D.; Whiteford, N.; Chen, C. H.; others The JWST early-release science program for direct observations of exoplanetary systems II: a 1 to 20  $\mu\text{m}$  spectrum of the planetary-mass companion VHS 1256–1257 b. *Astron. J. Lett.* **2023**, *946*, L6; (d) Rustamkulov, Z.; Sing, D.; Mukherjee, S.; May, E. M.; Kirk, J.; Schlawin, E.; Line, M. R.; Piaulet, C.; Carter, A. L.; Batalha, N. E.; others Early release science of the exoplanet WASP-39b with JWST NIRSpec PRISM. *Nature* **2023**, *614*, 659–663.
- (3) (a) Follmann, H.; Brownson, C. Darwin's warm little pond revisited: from molecules to the origin of life. *Naturwissenschaften* **2009**, *96*, 1265–1292; (b) Deamer, D. Salty seawater or a warm little pond: where did life begin? *Academia Letters* **2020**, *105*.
- (4) Westall, F.; Brack, A.; Fairén, A. G.; Schulte, M. D. Setting the geological scene for the origin of life and continuing open questions about its emergence. *Front. Astron. Space Sci.* **2023**, *9*, 1095701.
- (5) (a) Lahav, N.; Chang, S. The possible role of solid surface area in condensation reactions during chemical evolution: reevaluation. *J. Mol. Evol.* **1976**, *8*, 357–380; (b) Dass, A. V.; Hickman-Lewis, K.; Brack, A.; Kee, T. P.; Westall, F. Stochastic prebiotic chemistry within realistic geological systems. *ChemistrySelect* **2016**, *1*, 4906–4926.
- (6) (a) Anders, E. Pre-biotic organic matter from comets and asteroids. *Nature* **1989**, *342*,

- 255–257; (b) Chyba, C.; Sagan, C. Endogenous production, exogenous delivery and impact-shock synthesis of organic molecules: an inventory for the origins of life. *Nature* **1992**, *355*, 125–132; (c) Walton, C. R.; Rigley, J. K.; Lipp, A.; Law, R.; Suttle, M. D.; Schönbächler, M.; Wyatt, M.; Shorttle, O. Cosmic dust fertilization of glacial prebiotic chemistry on early Earth. *Nat. Astron.* **2024**, 1–11.
- (7) (a) Sephton, M. A. Organic compounds in carbonaceous meteorites. *Nat. Prod. Rep.* **2002**, *19*, 292–311; (b) Sandford, S. A. Terrestrial analysis of the organic component of comet dust. *Annu. Rev. Anal. Chem.* **2008**, *1*, 549–578; (c) Potapov, A.; McCoustra, M. Physics and chemistry on the surface of cosmic dust grains: a laboratory view. *Int. Rev. Phys. Chem.* **2021**, *40*, 299–364.
- (8) Camprubi, E.; De Leeuw, J.; House, C.; Raulin, F.; Russell, M.; Spang, A.; Tirumalai, M.; Westall, F. The emergence of life. *Space Sci. Rev.* **2019**, *215*, 1–53.
- (9) Hazen, R. M.; Sverjensky, D. A.; Azzolini, D.; Bish, D. L.; Elmore, S. C.; Hinnov, L.; Milliken, R. E. Clay mineral evolution. *Am. Mineral.* **2013**, *98*, 2007–2029.
- (10) Zhao, T.; Xu, S.; Hao, F. Differential adsorption of clay minerals: implications for organic matter enrichment. *Earth-Sci. Rev.* **2023**, *246*, 104598.
- (11) Nagendrappa, G.; Chowreddy, R. R. Organic reactions using clay and clay-supported catalysts: a survey of recent literature. *Catal. Surv. Asia* **2021**, *25*, 231–278.
- (12) Poulet, F.; Bibring, J.-P.; Mustard, J.; Gendrin, A.; Mangold, N.; Langevin, Y.; Arvidson, R.; Gondet, B.; Gomez, C. Phyllosilicates on Mars and implications for early Martian climate. *Nature* **2005**, *438*, 623–627.
- (13) (a) Bernal, J. D. The physical basis of life. *Proc. Phys. Soc., London, Sect. B* **1949**, *62*, 752; (b) Cairns-Smith, A. G. *Seven clues to the origin of life: a scientific detective story*; Cambridge University Press: Shaftesbury Road, Cambridge CB2 8EA, UK, 1990;

- (c) Hazen, R. M.; Sverjensky, D. A. Mineral surfaces, geochemical complexities, and the origins of life. *Cold Spring Harbor Perspect. Biol.* **2010**, *2*, a002162.
- (14) (a) Lambert, J.-F. Adsorption and polymerization of amino acids on mineral surfaces: a review. *Origins Life Evol. Biospheres* **2008**, *38*, 211–242; (b) Yu, W. H.; Li, N.; Tong, D. S.; Zhou, C. H.; Lin, C. X. C.; Xu, C. Y. Adsorption of proteins and nucleic acids on clay minerals and their interactions: a review. *Appl. Clay Sci.* **2013**, *80*, 443–452; (c) Kloprogge, J. T.; Hartman, H. Clays and the origin of life: The experiments. *Life* **2022**, *12*, 259; (d) Millman, E.; Chatterjee, A.; Parker, K. M.; Catalano, J. G. Cation exchange to montmorillonite induces selective adsorption of amino acids. *Geochim. Cosmochim. Acta* **2024**,
- (15) Bala, P.; Samantaray, B.; Srivastava, S. Dehydration transformation in Ca-montmorillonite. *Bull. Mater. Sci.* **2000**, *23*, 61–67.
- (16) (a) Lahav, N.; White, D.; Chang, S. Peptide formation in the prebiotic era: thermal condensation of glycine in fluctuating clay environments. *Science* **1978**, *201*, 67–69; (b) Fuchida, S.; Masuda, H.; Shinoda, K. Peptide formation mechanism on montmorillonite under thermal conditions. *Origins Life Evol. Biospheres* **2014**, *44*, 13–28; (c) Fox, S.; Pleyer, H. L.; Strasdeit, H. An automated apparatus for the simulation of prebiotic wet–dry cycles under strictly anaerobic conditions. *Int. J. Astrobiol.* **2019**, *18*, 60–72.
- (17) Jaber, M.; Georgelin, T.; Bazzi, H.; Costa-Torro, F.; Lambert, J.-F.; Bolbach, G.; Clodic, G. Selectivities in adsorption and peptidic condensation in the (arginine and glutamic acid)/montmorillonite clay system. *J. Phys. Chem. C* **2014**, *118*, 25447–25455.
- (18) (a) Huang, W.; Ferris, J. P. One-step, regioselective synthesis of up to 50-mers of RNA oligomers by montmorillonite catalysis. *J. Am. Chem. Soc.* **2006**, *128*, 8914–8919; (b) Joshi, P. C.; Dubey, K.; Aldersley, M. F.; Sausville, M. Clay catalyzed RNA synthesis

- under Martian conditions: application for Mars return samples. *Biochem. Biophys. Res. Commun.* **2015**, *462*, 99–104.
- (19) Namani, T.; Snyder, S.; Eagan, J. M.; Bevilacqua, P. C.; Wesdemiotis, C.; Sahai, N. Amino acid specific nonenzymatic montmorillonite-promoted RNA polymerization. *ChemSystemsChem* **2021**, *3*, e2000060.
- (20) Ramos-Martinez, V.; Ramirez-Vargas, E.; Medellin-Rodriguez, F.; Ávila-Orta, C.; Gallardo-Vega, C.; Jasso-Salcedo, A.; Andrade-Guel, M. Zeolite 13X modification with gamma-aminobutyric acid (GABA). *Microporous Mesoporous Mater.* **2020**, *295*, 109941.
- (21) Zaia, D. A.; Zaia, C. T. B.; De Santana, H. Which amino acids should be used in prebiotic chemistry studies? *Origins Life Evol. Biospheres* **2008**, *38*, 469–488.
- (22) (a) Friebele, E.; Shimoyama, A.; Ponnamperuma, C. Adsorption of protein and non-protein amino acids on a clay mineral: a possible role of selection in chemical evolution. *J. Mol. Evol.* **1980**, *16*, 269–278; (b) Sato, M. Preparation of kaolinite-amino acid intercalates derived from hydrated kaolinite. *Clays Clay Miner.* **1999**, *47*, 793–802.
- (23) Block, K. A.; Trusiak, A.; Katz, A.; Alimova, A.; Wei, H.; Gottlieb, P.; Steiner, J. C. Exfoliation and intercalation of montmorillonite by small peptides. *Appl. Clay Sci.* **2015**, *107*, 173–181.
- (24) (a) Alexandre, M.; Dubois, P. Polymer-layered silicate nanocomposites: preparation, properties and uses of a new class of materials. *Mater. Sci. Eng., R* **2000**, *28*, 1–63; (b) Zhu, T. T.; Zhou, C. H.; Kabwe, F. B.; Wu, Q. Q.; Li, C. S.; Zhang, J. R. Exfoliation of montmorillonite and related properties of clay/polymer nanocomposites. *Appl. Clay Sci.* **2019**, *169*, 48–66; (c) Das, S.; Sharma, P.; Kumar, M.; Gupta, R. K.; Sharma, H.; others A review on clay exfoliation methods and modifications for CO<sub>2</sub> capture application. *Mater. Today Sustain.* **2023**, 100427.

- (25) Castellini, E.; Malferrari, D.; Bernini, F.; Brigatti, M. F.; Castro, G. R.; Medici, L.; Mucci, A.; Borsari, M. Baseline studies of the clay minerals society source clay montmorillonite STx-1b. *Clays Clay Miner.* **2017**, *65*, 220–233.
- (26) Suresh, D.; Sajan, D.; Laladas, K.; Joe, I. H.; Jayakumar, V. Vibrational spectra of gamma-aminobutyric acid. AIP Conference Proceedings. 2008; pp 95–97.
- (27) Buchbender, F.; Wiese, M. Efficient concentration of an amino acid using reactive extraction coupled with bipolar electrodialysis. *Chem. Eng. Technol.* **2018**, *41*, 2298–2305.
- (28) Madejova, J.; Komadel, P. Baseline studies of the clay minerals society source clays: infrared methods. *Clays Clay Miner.* **2001**, *49*, 410–432.
- (29) Farmer, V. C. *The Infrared Spectra of Minerals*, 4th ed.; Mineralogical Society of Great Britain and Ireland: 12 Baylis Mews, Wickenham, TW1 3HQ, 1974; Chapter 15, pp 331–363.
- (30) Cole, K. C. Use of infrared spectroscopy to characterize clay intercalation and exfoliation in polymer nanocomposites. *Macromolecules* **2008**, *41*, 834–843.
- (31) (a) Dong, F.; Guo, Y.; Liu, M.; Zhou, L.; Zhou, Q.; Li, H. Spectroscopic evidence and molecular simulation investigation of the bonding interaction between lysine and montmorillonite: implications for the distribution of soil organic nitrogen. *Appl. Clay Sci.* **2018**, *159*, 3–9; (b) Zhu, C.; Wang, Q.; Huang, X.; Yun, J.; Hu, Q.; Yang, G. Adsorption of amino acids at clay surfaces and implication for biochemical reactions: role and impact of surface charges. *Colloids Surf., B* **2019**, *183*, 110458.
- (32) Morgan, A. B.; Gilman, J. W. Characterization of polymer-layered silicate (clay) nanocomposites by transmission electron microscopy and X-ray diffraction: a comparative study. *J. Appl. Polym. Sci.* **2003**, *87*, 1329–1338.

- (33) Valášková, M.; Rieder, M.; Matějka, V.; Čapková, P.; Slíva, A. Exfoliation/delamination of kaolinite by low-temperature washing of kaolinite–urea intercalates. *Appl. Clay Sci.* **2007**, *35*, 108–118.
- (34) Usuki, A.; Kawasumi, M.; Kojima, Y.; Okada, A.; Kurauchi, T.; Kamigaito, O. Swelling behavior of montmorillonite cation exchanged for  $\omega$ -amino acids by  $\epsilon$ -caprolactam. *J. Mater. Res.* **1993**, *8*, 1174–1178.
- (35) Sánchez, F. G.; Jurányi, F.; Gimmi, T.; Van Loon, L.; Seydel, T.; Unruh, T. Dynamics of supercooled water in highly compacted clays studied by neutron scattering. *J. Phys.: Condens. Matter* **2008**, *20*, 415102.
- (36) Santagata, M.; Johnston, C. T. A study of nanoconfined water in halloysite. *Appl. Clay Sci.* **2022**, *221*, 106467.
- (37) Bergman, R.; Swenson, J. Dynamics of supercooled water in confined geometry. *Nature* **2000**, *403*, 283–286.
- (38) Zhang, C.; Liu, Z. Freezing of water confined in porous materials: role of adsorption and unfreezable threshold. *Acta Geotech.* **2018**, *13*, 1203–1213.
- (39) Yan, L.; Roth, C. B.; Low, P. F. Changes in the Si-O vibrations of smectite layers accompanying the sorption of interlayer water. *Langmuir* **1996**, *12*, 4421–4429.
- (40) (a) Maddams, W.; Mead, W. The measurement of derivative i.r. spectra — I. background studies. *Spectrochim. Acta, Part A* **1982**, *38*, 437–444; (b) Dong, A.; Huang, P.; Caughey, W. S. Protein secondary structures in water from second-derivative amide I infrared spectra. *Biochemistry* **1990**, *29*, 3303–3308.
- (41) Savitzky, A.; Golay, M. J. Smoothing and differentiation of data by simplified least squares procedures. *Anal. Chem.* **1964**, *36*, 1627–1639.

- (42) Martínez-Cagigal, V. Shaded area error bar plot , MATLAB Central File Exchange. 2023; <https://www.mathworks.com/matlabcentral/fileexchange/58262-shaded-area-error-bar-plot>.
- (43) Wells, J. `lorentzfit(x,y,varargin)`, MATLAB Central File Exchange. 2023; <https://www.mathworks.com/matlabcentral/fileexchange/33775-lorentzfit-x-y-varargin>.
- (44) Lavina, B.; Dera, P.; Downs, R. T. Modern X-ray diffraction methods in mineralogy and geosciences. *Rev. Mineral. Geochem.* **2014**, *78*, 1–31.